Insertable biplanar gradient coils for magnetic resonance imaging ⊘

M. A. Martens; L. S. Petropoulos; R. W. Brown; J. H. Andrews; M. A. Morich; J. L. Patrick
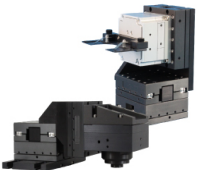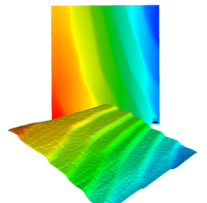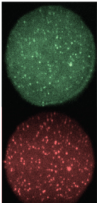
Check for updates

View Online

Export Citation

CrossMark

03 December 2023 13:22:56

AIP Publishing

Insertable biplanar gradient coils for magnetic resonance imaging

M. A. Martens, L. S. Petropoulos, R. W. Brown, and J. H. Andrews
Case Western Reserve University, Department of Physics, Cleveland, Ohio 44106-7079

M. A. Morich and J. L. Patrick
Picker International, Inc., Highland Heights, Ohio 44143

Insertable planar gradient coils offer the potential for significant performance increases in magnetic resonance imaging through higher gradient strength and shorter rise times. Using variational methods to minimize inductance, and thereby to optimize switching speeds, we have analyzed and constructed a biplanar y-gradient coil for insertion into a solenoidal magnet system where z is the magnet axis. We have also analyzed biplanar x-gradient and z-gradient coil designs using the same methods. These biplanar coils offer an advantage over a cylindrical coil of comparable diameter in that they achieve high gradient strengths with relatively short rise times while maintaining patient access. Although the requirement that the currents for the x gradient lie in the same plane as for the y and z gradients increases the stored energy by a factor of 3 with respect to the other two gradients, this stored energy is still smaller by a factor of 2 than that of a comparably constrained x-gradient cylindrical coil. The biplanar coil design offers improved linearity over its single planar coil alternative. The particular designs we have investigated are generally limited to small-volume imaging.

I. INTRODUCTION

The gradient requirements for echo planar imaging[1] or, more recently, snapshot imaging[2] are on the order of 10–40 mT/m with rise times on the order of 100 μs at the high end. Larger gradients and more rapid slew rates are also required for shorter echo times, the reduction of susceptibility artifacts in 2D and 3D imaging,[3] and for diffusion/perfusion imaging. These techniques will play a key role in future magnetic resonance imaging (MRI) sequences and machine design.

The improvement of gradient system performance through reduction of rise times, while maintaining patient access, should allow for the development of new imaging sequences. Specifically, using variational methods, Turner[1] has shown how optimal inductance coils, consistent with a given field specification, can be designed by minimizing the energy stored in the field. Minimization of the stored energy is to be carried out under certain design constraints such as strength, linearity, and patient aperture size. For a given rise-time requirement t_r and field gradient strength G, the stored energy will determine the gradient amplifier power requirements directly as $2W_m(G)/t_r$, where $W_m(G)$ is the stored magnetic energy at gradient strength G.

The dominant design variable in reducing stored energy for conventional cylindrical coils is scaling of the radius. In free space, at a constant gradient strength, the relationship between stored energy and coil radius is a fifth power law. Upon insertion into a superconducting magnet, the eddy current interaction increases this to an Nth power law ($N > 5$), where the value of N is now dependent upon the ratio of radii of the primary coil and the eddy current/radiation shield. Patient access constraints, however, limit the degree of scaling achievable. These limitations are different for head, body, or limb imaging.

Roemer[2] and Frollo[3] have previously detailed some of the benefits of the use of planar gradient coils to overcome scaling problems applicable to conventional cylindrical coils. Roemer first proposed the use of an insertable single planar surface gradient coil in medical solenoidal MRI equipment to achieve significant reductions in stored energy while maintaining patient access. The concept is a simple one: as one approaches the current sources the local gradient strength per unit ampere will increase. The price paid for this type of arrangement is in the highly nonlinear spatial behavior of the field. By analyzing and constructing a multiconductor parallel-plane gradient system (for use in MR spectrometers to image small biological objects), Frollo showed that it is possible to generate a linear gradient magnetic field of high intensity with a large inside volume. He used conductive strips with a known current distribution and varied the location of the imaging area in order to obtain the desired gradient field. While Frollo's approach optimized the linearity of the gradient field distribution within the imaging region, it did not systematically minimize the stored energy, and thus the inductance, of the coil design. Unlike the design we present here, his design did not minimize the time required for switching magnetic fields.

Our work combines the ideas of Turner and Roemer to develop an optimal biplanar gradient coil design strategy for controlling x-, y-, and z-gradient fields. In this article we use an extension to the inverse method as proposed by Turner for cylindrical coil design to minimize induction for a given gradient field. Turner applied minimization techniques to the analysis of cylindrical coils. We extend that work to apply it to biplanar coils. This strategy yields a
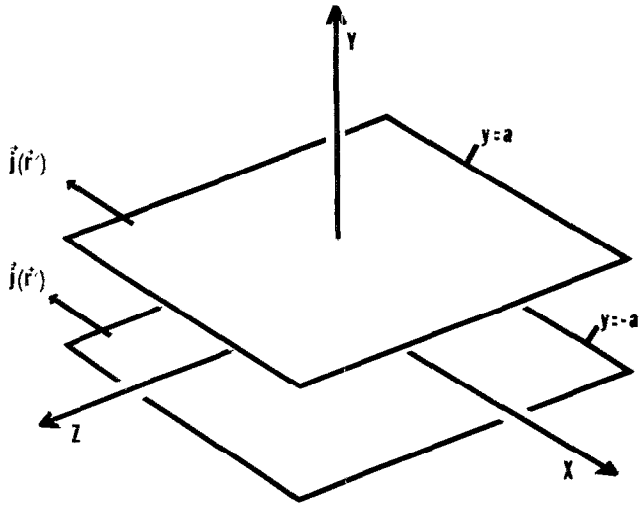
FIG. 1. Geometry and orientation of the planar coils. The sheets are infinite in the x and z directions.

design with good linearity for imaging, shorter rise times, and smaller eddy currents; the high performance required for microscopy and real-time imaging techniques, and reduced stored energy requirements for operation. Insertability of the biplanar coils into an existing MRI system was a major consideration in the development of this design strategy. The work of some of the authors on the design and construction of biplanar coils for a y-gradient field has been previously reported.[4]

II. THEORY

We are interested in producing a magnetic field with its z component having the desired gradient behavior along either the x, y, or z directions. The solenoid main magnet axis is the z axis. To produce the desired gradient field, we demand that the current densities lie on two parallel planes at $y = a$ and $y = -a$ as shown in Fig. 1. The current densities can then be expressed in the following form:

$$
\mathbf{J}(\mathbf{r}) = [J_x^a(x,z)\hat{x} + J_z^a(x,z)\hat{z}]\delta(y - a)
$$

$$
+ [J_x^{-a}(x,z)\hat{x} + J_z^{-a}(x,z)\hat{z}]\delta(y + a). \tag{1}
$$

The calculation of the magnetic fields and stored magnetic energy due to these currents is made easier by the appropriate choice of a Green function expansion. For our purpose the best choice is

$$
G(\mathbf{r},\mathbf{r}') = \frac{1}{|\mathbf{r} - \mathbf{r}'|}
$$

$$
= \frac{1}{2\pi} \int_{-\infty}^{\infty} \int_{-\infty}^{\infty} \frac{d\alpha \, d\beta}{\sqrt{\alpha^2 + \beta^2}} e^{i\alpha(x - x')}
$$

$$
\times e^{i\beta(z - z')} e^{-\sqrt{\alpha^2 + \beta^2}(y_> - y_<)}, \tag{2}
$$

where $y_>$ ($y_<$) is the greater (lesser) of y and y'. It is also convenient to define the Fourier transform pair of the components of the current density as follows:

$$
j_x^a(\alpha,\beta) = \int_{-\infty}^{\infty} \int_{-\infty}^{\infty} dx \, dz e^{-i\alpha x} e^{-i\beta z} J_x^a(x,z),
$$

$$
J_x^a(x,z) = \frac{1}{4\pi^2} \int_{-\infty}^{\infty} \int_{-\infty}^{\infty} d\alpha \, d\beta e^{i\alpha x} e^{i\beta z} j_x^a(\alpha,\beta), \tag{3}
$$

and similarly for the other components. We note here that the continuity equation for the current densities,

$$
\nabla \cdot \mathbf{J}(\mathbf{r}) = 0 \tag{4}
$$

can be used to relate the two components of the current,

$$
\alpha j_x^a(\alpha,\beta) + \beta j_z^a(\alpha,\beta) = 0. \tag{5}
$$

We proceed to calculate the vector potential by using (2) and (3) in the expression

$$
\mathbf{A}(\mathbf{r}) = \frac{\mu_0}{4\pi} \int_V \frac{\mathbf{J}(\mathbf{r}')}{|\mathbf{r} - \mathbf{r}'|} d^3x'. \tag{6}
$$

It is easy to see how the integrals over x and z convert the components of the current densities into their corresponding Fourier transform components. As a result of these substitutions and transformations we obtain, for $y < a$,

$$
A_x(\mathbf{r}) = \frac{\mu_0}{8\pi^2} \int_{-\infty}^{\infty} \int_{-\infty}^{\infty} \frac{d\alpha \, d\beta}{\sqrt{\alpha^2 + \beta^2}} e^{i\alpha x} e^{i\beta z}
$$

$$
\times [e^{-\sqrt{\alpha^2 + \beta^2}(a - y)} j_x^a(\alpha,\beta)
$$

$$
+ e^{-\sqrt{\alpha^2 + \beta^2}(a + y)} j_x^{-a}(\alpha,\beta)], \tag{7}
$$

$$
A_z(\mathbf{r}) = \frac{\mu_0}{8\pi^2} \int_{-\infty}^{\infty} \int_{-\infty}^{\infty} \frac{d\alpha \, d\beta}{\sqrt{\alpha^2 + \beta^2}} e^{i\alpha x} e^{i\beta z}
$$

$$
\times [e^{-\sqrt{\alpha^2 + \beta^2}(a - y)} j_z^a(\alpha,\beta)
$$

$$
+ e^{-\sqrt{\alpha^2 + \beta^2}(a + y)} j_z^{-a}(\alpha,\beta)], \tag{8}
$$

$$
A_y(\mathbf{r}) = 0. \tag{9}
$$

The z component of the magnetic field is now calculated from the vector potential,

$$
B_z(\mathbf{r}) = -\frac{\mu_0}{8\pi^2} \int_{-\infty}^{\infty} \int_{-\infty}^{\infty} d\alpha \, d\beta e^{i\alpha x} e^{i\beta z}
$$

$$
\times [e^{\sqrt{\alpha^2 + \beta^2}(y - a)} j_x^a(\alpha,\beta)
$$

$$
- e^{-\sqrt{\alpha^2 + \beta^2}(y + a)} j_x^{-a}(\alpha,\beta)]. \tag{10}
$$

The total stored magnetic energy must also be expressed in terms of the current densities. Starting with

$$
W = \frac{1}{2} \int_V \mathbf{A} \cdot \mathbf{J} \, d^3x, \tag{11}
$$

and making the proper substitutions we arrive at

$$W = \frac{\mu_0}{16\pi^2} \int_{-\infty}^{\infty} \int_{-\infty}^{\infty} \frac{d\alpha \, d\beta}{\sqrt{\alpha^2 + \beta^2}} \left(1 + \frac{\alpha^2}{\beta^2}\right) \{ \, | \, j_x^{\,a}(\alpha,\beta) \, |^2$$

$$+ \, | \, j_x^{-a}(\alpha,\beta) \, |^2$$

$$+ \, e^{-2a\sqrt{\alpha^2+\beta^2}} [\, j_x^{\,a}(\alpha,\beta) \, j_x^{-a*}(\alpha,\beta)$$

$$+ \, j_x^{\,a*}(\alpha,\beta) \, j_x^{-a}(\alpha,\beta) \,] \}, \tag{12}$$

where * denotes complex conjugation.

Since the purpose is to design a gradient field with a linear z component, the currents should be constrained so that the B_z is sufficiently linear. To do this, the axial magnetic field is specified to take on certain values at different points in the imaging region. These constraints on the field are expressed as

$$B_z(\mathbf{r}_i) = \mathcal{B}_{z,i} \quad \text{for } i = 1,N, \tag{13}$$

where there are N points, $\mathbf{r}_i$, at which the field is constrained to have the values $\mathcal{B}_{z,i}$.

We are now ready to construct the energy functional $E[\, j_x^{\,a}(\alpha,\beta), j_x^{-a}(\alpha,\beta)]$ which will then be extremized to give the desired current density. Before proceeding, however, matters can be greatly simplified by considering the symmetry of the problem with respect to the y coordinate. If the z-component magnetic field that we desire is antisymmetric about the $y = 0$ plane, then the current densities must be symmetric, $j_x^{\,a}(\alpha,\beta) = j_x^{-a}(\alpha,\beta)$, and if the z component of the magnetic field is symmetric, the current densities must be antisymmetric, $j_x^{\,a}(\alpha,\beta) = -j_x^{-a}(\alpha,\beta)$.

Using these relations, simplified expressions for B_z and W are derived. For antisymmetric fields (symmetric current densities), we obtain

$$B_z(\mathbf{r}) = -\frac{\mu_0}{4\pi^2} \int_{-\infty}^{\infty} \int_{-\infty}^{\infty} d\alpha \, d\beta e^{i\alpha x}$$

$$\times e^{i\beta z} j_x^{\,a}(\alpha,\beta) e^{-a\sqrt{\alpha^2+\beta^2}} \sinh(y\sqrt{\alpha^2+\beta^2}) \tag{14}$$

$$W = \frac{\mu_0}{4\pi^2} \int_{-\infty}^{\infty} \int_{-\infty}^{\infty} \frac{d\alpha \, d\beta}{\sqrt{\alpha^2+\beta^2}} \left(1 + \frac{\alpha^2}{\beta^2}\right)$$

$$\times | \, j_x^{\,a}(\alpha,\beta) \, |^2 e^{-a\sqrt{\alpha^2+\beta^2}} \cosh(a\sqrt{\alpha^2+\beta^2}). \tag{15}$$

The constrained energy functional E is now constructed,

$$E[\, j_x^{\,a}(\alpha,\beta)] = W - \sum_{j=1}^{N} \lambda_j \, [B_z(\mathbf{r}_j) - \mathcal{B}_{z,j}], \tag{16}$$

and its variation with respect to $j_x^{\,a}(\alpha,\beta)$ is set to zero. Using the simplified relations, the current density is found to be

$$j_x^{\,a*}(\alpha,\beta) = -\frac{\beta^2}{2\sqrt{\alpha^2+\beta^2}\cosh(a\sqrt{\alpha^2+\beta^2})} \sum_{j=1}^{N} \lambda_j$$

$$\times e^{i\alpha x_j} e^{i\alpha z_j} \sinh(y_j\sqrt{\alpha^2+\beta^2}). \tag{17}$$

With the form of the current density given, the next step is to calculate the values of the Lagrange multipliers, λ_j. By substituting the current density into the expression for the

magnetic field and then using the constraint relations (13), the following matrix equation is arrived at:

$$\mathcal{B}_{z,i} = \sum_{j=1}^{N} C_{ij}\lambda_j \quad \text{for } i = 1,N, \tag{18}$$

where, for the antisymmetric case,

$$C_{ij} = -\frac{\mu_0}{8\pi^2} \int_{-\infty}^{\infty} \int_{-\infty}^{\infty} \frac{\beta^2 e^{-a\sqrt{\alpha^2+\beta^2}}}{\sqrt{\alpha^2+\beta^2}\cosh(a\sqrt{\alpha^2+\beta^2})}$$

$$\times \sum_{j=1}^{N} e^{i\alpha x_i} e^{-i\alpha x_j} e^{i\beta z_i} e^{-i\beta z_j} \sinh(y_i\sqrt{\alpha^2+\beta^2})$$

$$\times \sinh(y_j\sqrt{\alpha^2+\beta^2}). \tag{19}$$

For the case of a symmetric field z component corresponding to an antisymmetric current density, the expressions for the magnetic field, the stored energy, the current densities, and the matrix coefficients can be obtained from the expressions for the antisymmetric z-component case by switching all cosh and sinh in Eqs. (14), (15), (17), and (19). In either case, the magnetic field and the stored magnetic energy are functionals of $j_x^{\,a}(\alpha,\beta)$ and $j_x^{\,a*}(\alpha,\beta)$ only.

These equations can be simplified further if the symmetries of the x and z coordinates are also taken into account. This will be done in following section where we design x-, y-, and z-gradient coils using this theory.

III. DESIGN

We now proceed to design x-, y-, and z-gradient coils. The geometry will be as in Fig. 1. The gradient will be such that the z component of the magnetic field is approximately linear in x, y, or z, respectively. The equations that were presented previously can be simplified further by noting that B_z will be antisymmetric about the normal plane of the direction of the gradient and symmetric about the other orthogonal directions. Thus for the y-gradient design, B_z will be symmetric about the $x = 0$ and $z = 0$ planes. In this instance, the result of this simplification is that all of the $e^{\pm i\alpha x}$ and $e^{\pm i\beta z}$ terms in Eqs. (3), (14), (15), (17), and (19) are replaced by $\cos(\alpha x)$ and $\cos(\beta z)$. Similarly, for the x-gradient (z-gradient) designs, the appropriate $e^{\pm i\alpha x}$ and $e^{\pm i\beta z}$ terms become $\pm i\sin(\alpha x)$ and $\cos(\beta z)[\cos(\alpha x)$ and $\pm i\sin(\beta z)]$, respectively. When specifying the constraints, only points in one octant need be given; seven other sets of constraints with the proper symmetries will be implied.

To design the x-, y-, and z-gradient coils, the first step was to choose the size of the coils and the sets of constraints. In each case, the separation between the two par-

TABLE I. Constraint points used for designing x-gradient planar coils. Values for x, y, and z are in meters; values for $\mathcal{B}_{z,i}$ are in milliTesla.

x_i	y_i	z_i	$\mathcal{B}_{z,i}$
0.001	0.000	0.000	0.040
0.001	0.125	0.000	0.032
0.125	0.000	0.000	4.500
0.001	0.000	0.125	0.032

TABLE II. Constraint points used for designing y-gradient planar coils. Values for x, y, and z are in meters; values for $\mathscr{B}_{z,i}$ are in milliTesla.

x_i	y_i	z_i	$\mathscr{B}_{z,i}$
0.000	0.001	0.000	0.040
0.000	0.125	0.000	4.500
0.125	0.001	0.000	0.032
0.000	0.001	0.125	0.032

allel planes was fixed at $2a = 44.72$ cm. This allows sufficient space of patient access and insertion of the coil within the typical physical constraints of a whole-body scanner. Sets for constraints that give suitable gradient fields for each direction and were used for this design study are given in Tables I, II, and III. These constraints specify a 40 mT/m gradient strength, 10% on-axis linearity out to 12.5 cm and 20% off-axis uniformity out to 12.5 cm.

Using these constraints, the current densities $J_x^a(x,z)$ and $J_z^a(x,z)$ were calculated. A contour representation of each of the current densities is shown in Figs. 2, 3, and 4. The method for generating these plots is discussed here since it is relevant to the process of discretizing the current densities for construction. From the continuum solution for the current densities one may construct a discrete coil through use of a stream function $S(x,y)$. Since the divergence of the coils is equal to zero, $\nabla \cdot \mathbf{J} = 0$, the current can be expressed as the curl of some vector function $\mathbf{S}(\mathbf{r})$, so that $\mathbf{J}(\mathbf{r}) = \nabla \times \mathbf{S}(\mathbf{r})$. For the present case, where the current is restricted to a two-dimensional surface, we need only be concerned with S_y. Then we have the result,

$$J_x^a(x,z)\hat{x} + J_z^a(x,z)\hat{z} = -\frac{\partial S_y}{\partial z}\hat{x} + \frac{\partial S_y}{\partial x}\hat{z}, \quad (20)$$

and S_y can be calculated from

$$S_y(x,z) = -\int_{-\infty}^{z} dz' \, J_x^a(x,z'). \quad (21)$$

Contour plots of the current densities are then generated by plotting the set of curves

$$S_y(x,z) = n\Delta S_y \quad \text{for } n = 1, N, \quad (22)$$

where N and ΔS_y will determine the number of contours and the magnitude of the current represented by each. Contours of constant ΔS_y represent equal two-dimensional intervals of integrated current which may be used to constitute discrete wire placement for the coil. The next step in the design process is to convert these continuous current densities into discrete wire positions. This was done using

TABLE III. Constraint points used for designing y-gradient planar coils. Values for x, y, and z are in meters; values for $\mathscr{B}_{z,i}$ are in milliTesla.

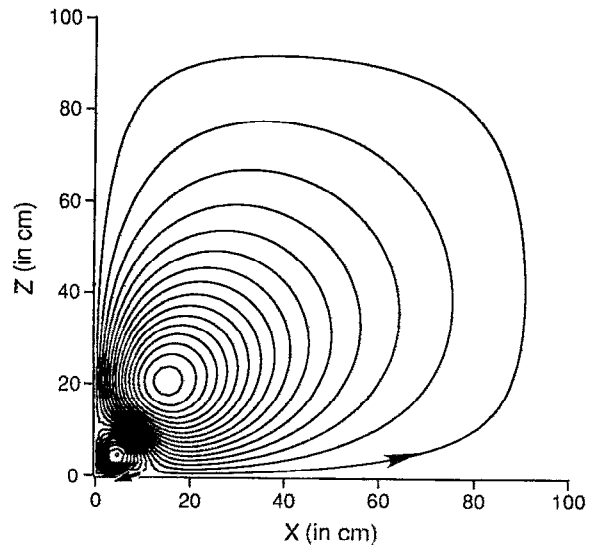| x_i	y_i	z_i	$\mathscr{B}_{z,i}$
0.000	0.000	0.001	0.040
0.000	0.125	0.001	0.032
0.125	0.000	0.001	0.032
0.000	0.000	0.125	4.500

FIG. 2. One quadrant of the current distribution of the planar x-gradient coil. Each contour line would carry a current of 329 A. The arrows indicate the flow of the current in each section.

the plot of contours of constant ΔS_y as just described. For each gradient direction, the positions of the wires will be the same as the contour lines as shown in Figs. 2, 3, and 4.

Once this discretization process was completed, the magnetic field from these wires was calculated using the Biot–Savart law. This procedure was cross checked and discretization effects were investigated by comparing the B_z field for 4, 8, 12, and 16 turn implementations of a biplanar y-gradient coil against that for the continuous current dis-
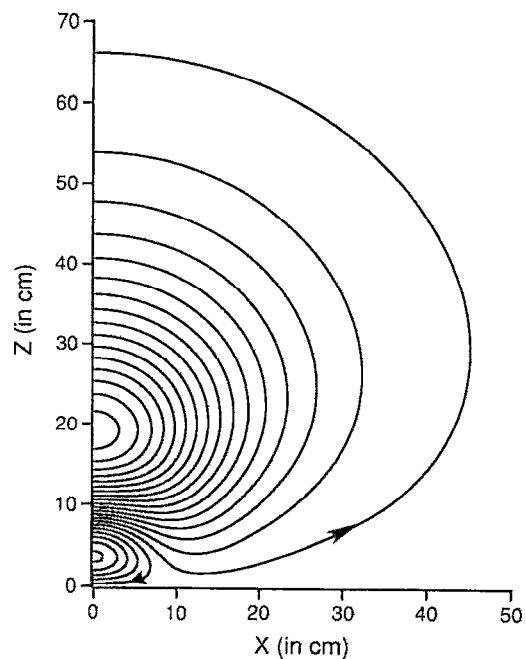

FIG. 3. One quadrant of the current distribution of the planar y-gradient coil. Each contour line would carry a current of 336 A. The arrows indicate the flow of the current in each section.
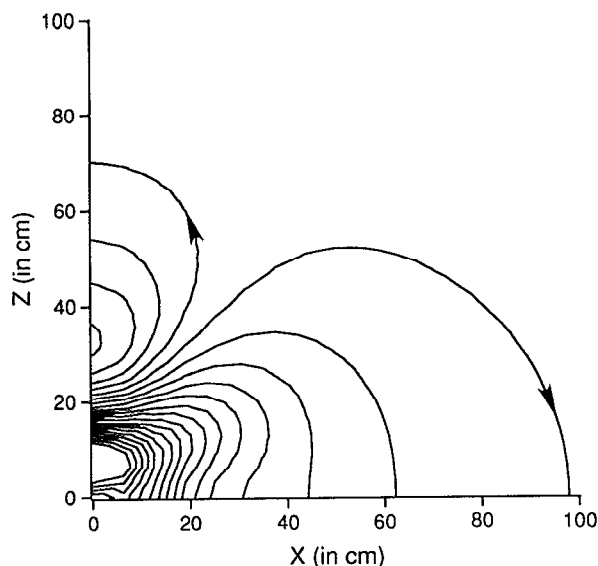
FIG. 4. One quadrant of the current distribution of the planar z-gradient coil. Each contour line would carry a current of 455 A. The arrows indicate the flow of the current in each section.

tribution. This is illustrated in Table IV. We find an excellent agreement between the 16-turn discrete and continuous implementations, as illustrated. Contour plots of B_z for each gradient design are shown in Figs. 5, 6, and 7. Within a circular slice of radius 12.5 cm, the magnetic field is linear to within 20% for the x-, y-, and z-gradient designs. The energy requirements for producing these fields are 34.969, 12.885, and 13.806 J, respectively.

Compared to the y- and z-gradient designs, we found that the energy requirements for the x-gradient design were threefold higher and thus present a practical design limitation. Because the current density for the x gradient is required to lie on the plane perpendicular to the x direction, it is difficult to generate current loops that can produce an antisymmetric gradient field in the x direction. The design of such a coil results in an increase in the stored energy needed for a specified x-gradient B_z to three times that of the y- and z-gradient coils and limits the effectiveness of the x-gradient coils in an existing MRI cylindrical scanner.

TABLE IV. Comparison of B_z (in mT) for y-gradient planar model coil for the continuous and various discrete current distributions at $y = 12.5$ cm away from the center.

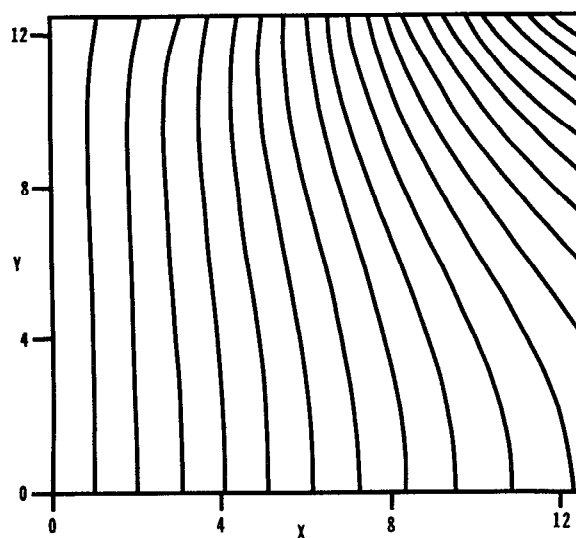| z in cm	Continuous	Discrete positive turns			
		4	8	12	16
10	6.7440	6.7966	6.7573	6.7497	6.7440
20	1.0553	1.0488	1.0523	1.0541	1.0553
30	− 3.4960	− 3.5304	− 3.5007	− 3.4964	− 3.4960
40	− 3.3124	− 3.2795	− 3.3138	− 3.3122	− 3.3126
50	− 1.9318	− 2.6455	− 1.9187	− 1.9307	− 1.9321
60	− 0.9595	− 0.8353	− 1.2631	− 1.0786	− 0.9595
70	− 0.4939	− 0.1046	− 0.2900	− 0.4272	− 0.4939

FIG. 5. Contour plot of B_z in the $z = 0$ plane for the x-gradient coil. Contours are at every 0.407 mT.

When we constrained the B_z field only to have the 40 mT/m gradient at the origin, but not to be otherwise constrained to the values in Tables I, II, and III, the energy requirements were greatly reduced to the values 23.04, 6.138, and 7.68 J, respectively. Although the energies are reduced, the uniformity of the field is also reduced.

The design strategy can be modified to reduce the physical size of the resulting coils by the use of Gaussian tapering in the spatial domain. As can be seen in Figs. 2, 3, and 4, the last several turns of the design extend relatively far along the x direction. By tapering the continuous current density before discretization, the size of the coil can be reduced in this direction, allowing for greater compatibility for insertion into an MRI cylindrical scanner. Since the current is predominantly z directed in the y- and z-gradient
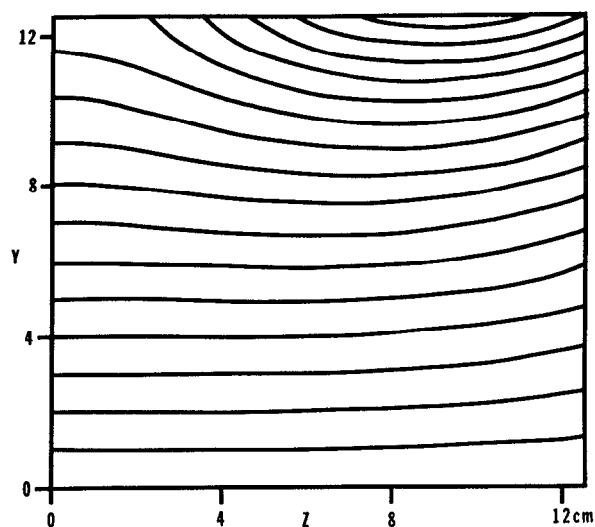

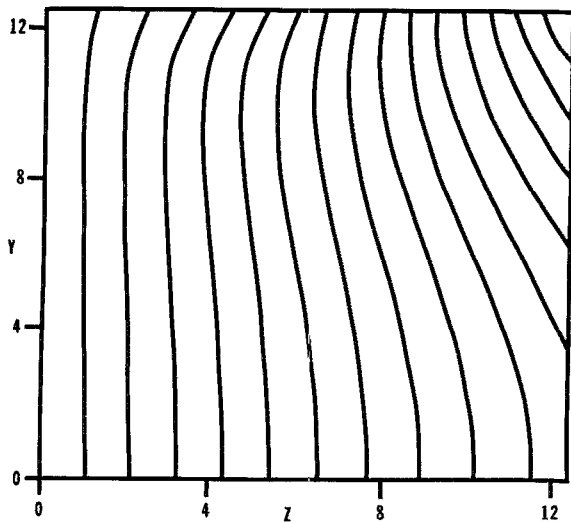FIG. 6. Contour plot of B_z in the $x = 0$ plane for the y-gradient coil. Contours are at every 0.400 mT.

FIG. 7. Contour plot of B_z in the $x = 0$ plane for the z-gradient coil. Contours are at every 0.435 mT.

FIG. 8. Gaussian x-tapered version of the x-gradient coil design in Fig. 2. Tapering was performed in the x direction only as noted in the text. The arrows indicate the flow of the current in each section.

cases in this region, the net effect on the B_z field will be minimal. Tapering the current J_x is also achievable for the x-gradient coil. Since the original current loops close in one quadrant, as shown in Fig. 2, tapering has the unwelcome effect of reducing the gradient strength due to the significant change of the shape of the current loops. The tapering scheme used does not alter the magnitude of the current per contour line for any gradient direction analyzed.

The Gaussian tapering algorithm used is as follows:

$$ J_x(x,z) = \begin{cases} J_x(x,z)e^{-\gamma^2(|x|-x_0)^2} & |x| \geqslant x_0 \\ J_x(x,z) & |x| < x_0 \end{cases}. $$

For $\gamma \sim 0.055$ cm^{-1} and $x_0 \sim 10.0$ cm we obtained a tapered version of the optimal x-gradient coil design discussed above, as shown in Fig. 8. The B_z field was checked on axis for the tapered coil out to 12.5 cm at which point the field was reduced to 43.6% of that produced by the untapered optimal coil. For $\gamma \sim 0.064$ cm^{-1} and $x_0 \sim 8.8$ cm, we obtained a tapered version of the optimal y-gradient coil design discussed above, as shown in Fig. 9. The B_z field was checked on axis for the tapered coil out to 12.5 cm. The fields were within 5% of those produced by the untapered optimal coil. For $\gamma \sim 0.055$ cm^{-1} and $x_0 \sim 10.0$ cm, we obtained a tapered version of the optimal z-gradient coil design discussed above, as shown in Fig. 10. The B_z field was checked on axis for the tapered coil out to 12.5 cm. The fields were within 6% of those produced by the untapered optimal coil.

To further test our theory and design techniques, a half-scale model of the y-gradient coil was constructed and tested. This model will be discussed in the next section.

IV. RESULTS

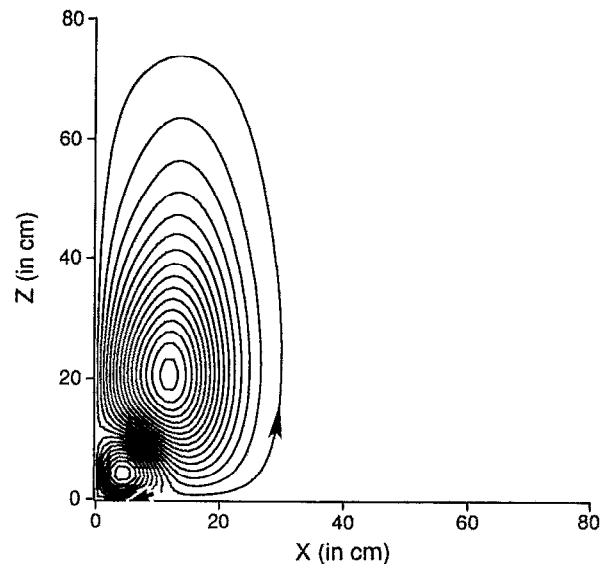In this section, we give the results from testing a half-scale model of the y-gradient coil designed in the previous section. This model was constructed and tested to validate the theory and verify that our calculations were correct. To build the scale model, loops of 1.02 mm diameter, No. 18 AWG wire were fastened to two pieces of wood. The loops were wound in series and placed in positions shown in Fig. 3. The magnetic field profile was measured using a search coil. (The search coil consisted of 200±5 turns of wire wrapped around a 15-mm-diam cylinder with a width of about 13 mm. The mean radius of the turns was estimated to be at 18 mm diameter.) The magnetic field was then
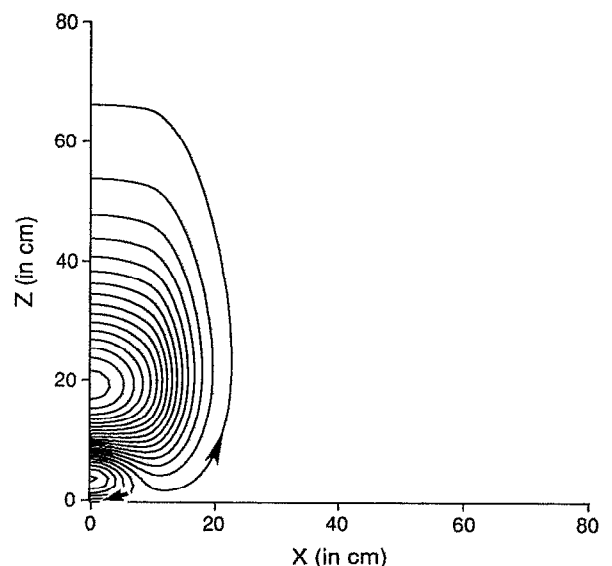

FIG. 9. Gaussian x-tapered version of the y-gradient coil design in Fig. 3. Tapering was performed in the x direction only as noted in the text. The arrows indicate the flow of the current in each section.
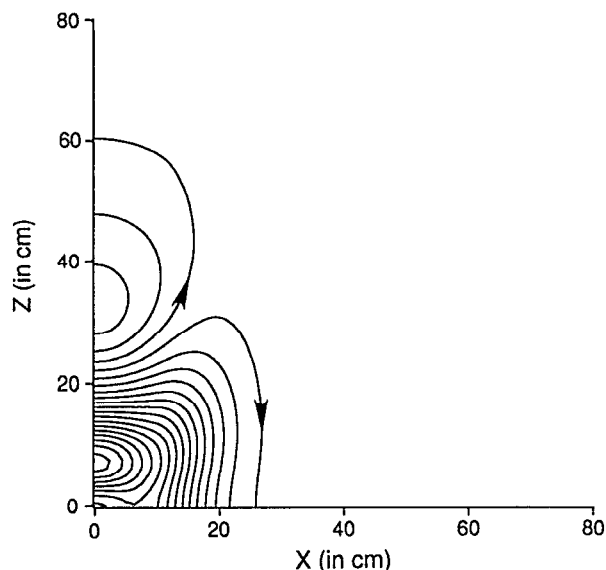
FIG. 10. Gaussian x-tapered version of the z-gradient coil design in Fig. 4. Tapering was performed in the x direction only as noted in the text. The arrows indicate the flow of the current in each section.

TABLE V. Measured B_z (in mT) for y-gradient planar model coil. Results are scaled to full scale with a current of 336 A.

	Y position			
	$y = 4$ cm	$y = 8$ cm	$y = 12$ cm	$y = 16$ cm
$x = 0$ cm	1.55	3.15	4.84	6.27
$x = 4$ cm	1.45	3.05	4.72	6.13
$x = 8$ cm	1.32	2.84	4.52	6.33
$x = 12$ cm	1.21	2.53	4.13	5.94
$x = 16$ cm	1.03	2.17	3.31	4.65
$x = 20$ cm	.80	1.68	2.64	3.41
$x = 24$ cm	.54	1.24	1.89	2.79
$x = 28$ cm	.41	.88	1.27	1.44
$x = 32$ cm	.28	.59	.83	.85
$x = 36$ cm	.22	.41	.54	.47
$x = 40$ cm	.13	.26	.34	.24

measured by driving the currents in the scale model with a sinusoidal current of frequency 10 kHz and a peak current of 2A. The results of these measurements in the $z = 0$ plane are shown in Table V for different values of x and y.

Plots of the results of these measurements versus calculated values, at several positions in the y direction, are shown in Fig. 11. These measurements confirm our theory and calculations to the level of 5%, which is within the accuracy of the measurements themselves.

The electrical characteristics of the coil were also measured. The coil's dc resistance was estimated to be 0.761 Ω based upon the net length of the wire used, its cross section, and the resistivity of the copper. The actual resistance was measured to be 0.7 Ω using a hand-held digital multimeter. To measure the inductance, we placed a 1 Ω sampling resistor in series with the coil (Dale Electronics, RH series wire-wound inductive, with inductance of ≈ 0.15 μH) for the purpose of measuring a sinewave current via an oscilloscope. We then supplied a 0.6 A peak, 10 kHz sinewave current, and measured a load voltage of 5.05 V peak. Knowing the dc resistance and response to the sinewave current, we obtained a measured inductance of 127 μH for the half-scale model. Since the inductance of a coil scales linearly with size, this would mean that a full scale gradient coil with this design would have an inductance of 254 μH. The expected coil inductance can be estimated from the calculated stored magnetic energy of the continuous current densities. Dividing this current density into 22 discrete wire loops we find that there will be 334 A in each loop. Since $W = \frac{1}{2}LI^2$ an approximate value for the inductance would be $L = 2 \times W/I^2 = 2 \times 12.89/(334)^2 = 231$ μH. Using the same formula for the stored energy W as in the y-gradient coil, we can evaluate the inductance for the x- and z-gradient coils. Knowing the value of the current for each current loop, the resulting inductance will be 646 and 133 μH for the x- and z-gradient design, respectively.

ACKNOWLEDGMENTS

FIG. 11. Plots of measured (markers) and calculated (lines) B_z vs x.

[1] R. Turner, J. Phys. E. **21**, 948 (1988).
[2] P. B. Roemer, SMRM Seventh Annual Meeting, Works in Progress, 1988.
[3] I. Frollo, Rev. Sci. Instrum. **60**, 3442 (1989).
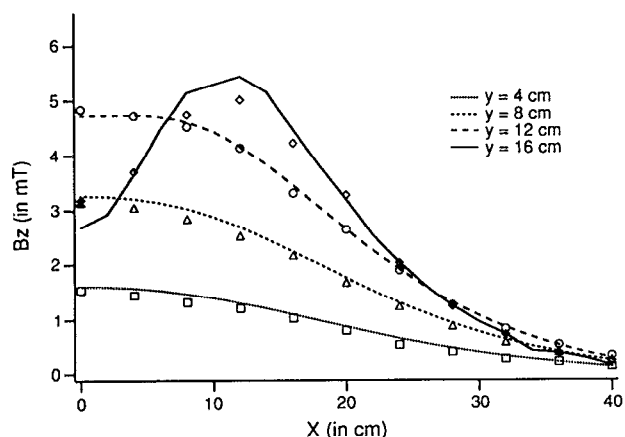[4] M. A. Morich, M. A. Martens, R. W. Brown, and J. L. Patrick, "Insertable Biplanar Gradient Coil for MR Imaging," SMRM Eighth Annual Meeting, Amsterdam, Poster 1989.